Check for updates

Space Weather

RESEARCH ARTICLE
10.1029/2021SW003017

Using Temporal Relationship of Thermospheric Density With Geomagnetic Activity Indices and Joule Heating as Calibration for NRLMSISE-00 During Geomagnetic Storms

Xin Wang[1,2,3], Juan Miao[1,3], Xian Lu[4], Ercha Aa[5], Binxian Luo[1,2,3], Ji Liu[6], Yu Hong[7], Yuxian Wang[1], Tingling Ren[1,2], Ruiyun Zeng[2], Chenxi Du[1,2,3], and Siqing Liu[1,2,3]

[1]National Space Science Center, Chinese Academy of Sciences, Beijing, China, [2]University of Chinese Academy of Sciences, Beijing, China, [3]Key Laboratory of Science and Technology on Environmental Space Situation Awareness, CAS, Beijing, China, [4]Department of Physics and Astronomy, Clemson University, Clemson, SC, USA, [5]Haystack Observatory, Massachusetts Institute of Technology, Westford, MA, USA, [6]Department of Physics, University of Alberta, Edmonton, AB, Canada, [7]Department of Physics, University of Texas at Arlington, Arlington, TX, USA

Abstract The responses of thermospheric densities to geomagnetic activity indices and Joule heating are analyzed during 265 geomagnetic storms and can be used to calibrate the model NRLMSISE-00 with neutral mass density observed at 400 km based on the CHAMP satellite from 2002 to 2008. In this work, the geomagnetic activities at high and low latitudes are identified by AE indices and Dst indices. During geomagnetic storms, Joule heating and its impacts on the thermospheric density are calculated by the Weimer-2001 electric potential model and the DMSP spacecraft. The results show that the response of thermospheric density to both AE and Dst index takes a longer time as geomagnetic storms intensify. During weak and moderate storms, density delays AE indices for about 0–1 hr, while it is 2–4 hr for intense storms. In addition, the time differences between Dst indices and AE indices increase as storms intensify. During weak and moderate geomagnetic storms, the difference in the time corresponding to Dst indices with the time when AE indices peak is only 1–2 hr, while it increases to 3–5 hr for the intense storms. Furthermore, the calibration of the NRLMSISE-00 model results can reproduce the storm-time thermospheric density well, with the Mean Relative Error (MRE) between density observation and model decreasing from 40% to 10% after the correction.

Plain Language Summary Thermospheric density, a major important factor affecting spacecraft operations, is influenced by geomagnetic activity and energy injection in the form of Joule heating. The most widely used model for the prediction of the neutral mass density is the NRLMSISE-00 model. In this study, the time relationships of thermospheric density with geomagnetic activity and Joule heating are statistically examined from 265 geomagnetic storms. These relationships can be used to correct the NRLMSISE-00 for better reproducing the storm-time density. It can be found that the response times of thermospheric density to Joule heating and geomagnetic activity increase as geomagnetic storms intensify. The density discrepancy between the NRLMSISE-00 model and observation can reach up to 40% of MRE during storms, however, the MRE between the calibration of the model and in-situ observed density decreases to 10%. Altogether, our results can contribute to understanding thermospheric variation of chemical composition and dynamics during geomagnetic storms and propose a method to calibrate the NRLMSISE-00 enhancing thermospheric density response for space weather applications.

Key Points:

- The responses of thermospheric density to geomagnetic activity indices and Joule heating take a longer time as geomagnetic storms intensify
- The density calibration for the NRLMSISE-00 model is developed as a function of Joule heating and geomagnetic activity indices during storms
- The calibration of the NRLMSISE-00 model can improve the simulation results of the storm-time density, with MRE decreasing from 40% to 10%

Correspondence to:
S. Liu and J. Miao,
liusq@nssc.ac.cn;
miaoj@nssc.ac.cn

Citation:
Wang, X., Miao, J., Lu, X., Aa, E., Luo, B., Liu, J., et al. (2022). Using temporal relationship of thermospheric density with geomagnetic activity indices and Joule heating as calibration for NRLMSISE-00 during geomagnetic storms. *Space Weather*, *20*, e2021SW003017. https://doi.org/10.1029/2021SW003017

Received 18 DEC 2021
Accepted 16 FEB 2022

Author Contributions:
Formal analysis: Juan Miao, Ji Liu, Yu Hong, Yuxian Wang
Investigation: Juan Miao, Ercha Aa
Methodology: Juan Miao, Xian Lu, Ercha Aa, Binxian Luo, Ji Liu, Siqing Liu
Resources: Juan Miao
Supervision: Juan Miao, Xian Lu, Ercha Aa, Binxian Luo, Siqing Liu
Validation: Juan Miao
Writing – original draft: Ji Liu, Yu Hong, Yuxian Wang, Tingling Ren, Ruiyun Zeng, Chenxi Du, Siqing Liu
Writing – review & editing: Xian Lu, Ercha Aa, Siqing Liu

© 2022. The Authors.
This is an open access article under the terms of the Creative Commons Attribution License, which permits use, distribution and reproduction in any medium, provided the original work is properly cited.

1. Introduction

The neutral mass density variation associated with the induced satellite drag force plays an important role in the Low Earth Orbit (LEO) spacecraft operations in the thermosphere, such as orbit maintenance, lifetime, and collision avoidance (Doornbos, 2012; Krauss et al., 2018; Zesta & Huang, 2016). Due to the impact of the solar-terrestrial energy input from the magnetosphere to the ionosphere-thermosphere system, the thermospheric density has intricate spatial and temporal variations. Consequently, predicting and simulating the neutral mass density changes and the related drag feedbacks to the spacecrafts are still a grand challenge for space weather research.

Since the 1950s, several empirical thermospheric density models have been applied for orbit determination and prediction of LEO spacecraft, such as Jacchia model and Mass Spectrometer Incoherent Scatter (MSIS) model (Jacchia, 1971; Hedin, 1987, 1991). However, the density discrepancies between the observations and these

models are about 15% in the quiet time (Bruinsma et al., 2004; Pardini et al., 2012; Vallado & Finkleman, 2014), and the errors can be much greater during geomagnetic storms (Bruinsma et al., 2006; Lei, Thayer, et al., 2011; Liu et al., 2005; Wang, Miao, Liu, & Ren, 2020, 2021). In addition, the US Naval Research Laboratory Mass Spectrometer and Incoherent Scatter Radar Extended (NRLMSISE-00) model is widely studied and utilized in space weather applications for predicting the satellite orbit (Picone et al., 2002). Satellites still lack in high-fidelity density observations due to current modeling uncertainties. Accelerometer-derived densities are indeed affected by systematic errors driven by the outer surface satellite geometry models (March et al., 2018), and simplified descriptions of the interactions between atmospheric particles and satellite surfaces (gas-surface interactions) (March et al., 2019, 2021; Moe & Moe, 2005). Other techniques can be used to derive thermospheric density (e.g., GPS-derived accelerations (Van den IJssel et al., 2020)), however, most of the time such alternatives cannot guarantee high-resolution output similarly to accelerometer-based measurements. Further enhancements in current thermosphere-ionosphere observation capabilities and dedicated missions would be necessary to improve current knowledge of dynamics and couplings in the thermosphere-ionosphere region (Palmroth et al., 2021).

During geomagnetic storms, the mass compositions and densities are determined by the solar-terrestrial energy dissipation through the coupled magnetosphere-ionosphere-thermosphere system (Aikio & Selkälä, 2009; Cai et al., 2013; Lei et al., 2008; Lu et al., 2016). Joule heating dominates two-thirds of the energy injection, and it can cause storm-time density increases at the high latitudes (Aikio et al., 2012; Cai et al., 2014; Knipp et al., 2004). The high-latitude heated neutral mass density expands upwards, contributing to the low-latitude thermospheric density disturbance due to the gravity waves and wind surges (Emmert, 2015; Lu et al., 2009; Oliveira et al., 2017; Wu et al., 2020). Further studies on the relationship between neutral mass density variation and Joule heating during the geomagnetic storms, therefore, are inevitable and important for the calibration of the thermospheric density model (Deng et al., 2009, 2013; Fedrizzi et al., 2012; Wang et al., 2021).

Furthermore, the different magnitudes of the geomagnetic storm can also lead to the storm-time variation of thermospheric density. Zesta and Oliveira (2019) found that the thermosphere response to geomagnetic storms varies because of the levels of storm intensity. Wang, Miao, Aa, et al. (2020) also concluded that thermospheric density increases strongly as geomagnetic storms intensify. The geomagnetic storm variations can be probed with geomagnetic activity indices, such as the auroral electrojet (AE) index representing the high latitudes, and the disturbed storm time (Dst) index identifying the low latitudes (Adebesin, 2016). The AE index is derived from several stations in the high latitude regions, especially in the auroral zone (Davis & Sugiura, 1966), and the Dst index obtained from several ground-based magnetometers at equatorial regions can measure the variations in the ring current (Sugiura, 1964). Thus, it is imperative to investigate the relationship of Joule heating (primary energy input), Dst (low-latitude geomagnetic activity indices), and AE (high-latitude geomagnetic activity indices) with storm-time thermospheric density.

The times for high-latitude and low-latitude geomagnetic activities reaching peaks are different during geomagnetic storms. During the period of 7–9 September 2017 geomagnetic storm, Zhang et al. (2019) reported that AE index peaks at about 23 UT on 7 September 2017, while Dst index peaks at about 02 UT on 8 September 2017. On 28 May 2011 storm, the high-latitude geomagnetic activity peaks at about 09 UT, while it peaks at about 11 UT in low latitudes (Wu et al., 2020). Using statistics data from 2000 to 2011, Maggiolo et al. (2017) concluded that the response time of geomagnetic activity indices to solar wind involves multiple timescales. In addition, the response times of thermospheric density to Joule heating vary with geomagnetic storm intensity changes. Due to the variance of altitudinal energy deposition, Wang, Miao, Aa, et al. (2020) discovered that thermospheric density delays Joule heating for a longer time as geomagnetic storms intensify. Therefore, the response times of neutral mass densities to Dst indices, AE indices, and Joule heating is of paramount significance to study thermospheric density enhancements during geomagnetic storms.

Recent studies have made great efforts to improve the thermospheric models (Ruan et al., 2018; Storz et al., 2005; Sutton et al., 2012; Weng et al., 2017). For the most widely applied model NRLMSISE-00, Zhou et al. (2009) concluded that the empirical relation regarding storm-time thermospheric density with the geomagnetic activities and Joule heating can correct the NRLMSISE-00 model and better predict neutral mass density. However, the temporal relationships of density to geomagnetic activity and Joule heating can also play a vital role in calibrating the NRLMSISE-00 model. In this study, 265 geomagnetic storms are statistically analyzed to investigate the time relationships of thermospheric density with Joule heating, Dst, and AE indices during geomagnetic storms.

These relationships can be utilized to calibrate the NRLMSISE-00 model to better simulate the storm-time thermospheric density.

This paper is organized as follows: the data processing is described in Section 2. The impacts of geomagnetic activity indices and Joule heating on thermospheric density observation and density discrepancy for a single storm are presented in Section 3.1. The statistical analysis following the case study in Section 3.1 is performed in Section 3.2 and Section 3.3. 90% of the geomagnetic storms are used to fit the function to calibrate the NRLMSISE-00 model as shown in Section 4. The verifications for the calibration model including assimilation results with these 90% of storms and the validation with the remaining 10% of storms are illustrated in Section 5. Finally, the summary and discussion are given in Section 6.

2. Data Processing

2.1. Thermospheric Density Enhancement

The Challenging Minisatellite Payload (CHAMP) satellite was launched on July 2000 with a near-circular orbit of 87.25° inclination at the height of 450 km (Reigber et al., 2002), and the Gravity Recovery and Climate Experiment (GRACE) satellite was launched on March 2002 with the inclination of 89.5° (Tapley et al., 2004). The accelerometer measurements onboard CHAMP and GRACE can measure thermospheric density with a time resolution of 10 and 5 s, leading to a spatial resolution of 80 and 40 km, respectively. The CHAMP and GRACE observed neutral mass densities can be obtained from TU Delft (Doornbos, 2012; March et al., 2021). In addition, Xu et al. (2011) found that the height differences between satellite apogee and perigee vary about 20–40 km in the orbits, and the satellite orbit also decays with time. This satellite height changes can lead to the variation of thermospheric density measurements, therefore, the method of Lei, Forbes, et al. (2011) and Xu et al. (2015) can be used to normalize CHAMP data to a reference height of 400 km,

$$\rho(h_0) = \frac{\rho(z) \times \rho_M(h_0)}{\rho_M(z)}, \tag{1}$$

where $\rho(h_0)$ is the neutral mass density at a normalized height h_0, $\rho(z)$ is the CHAMP observation at the satellite orbit height z, and ρ_M is the corresponding NRLMSISE-00 model thermospheric density.

To remove the effect of fluctuating solar radiation on thermospheric density from 2002 to 2008, the densities have been normalized to a constant solar radio flux, F10.7. Based on the quasi-linear relationship between solar radiation and thermospheric density (Wang et al., 2021), the F10.7 can be normalized to a reference level of 150 sfu, which is the median value of the solar radio flux for 265 geomagnetic storms, as used by Ma et al. (2010) and Miao et al. (2012):

$$\rho(F_0) = \frac{\rho(F) \times \rho_M(F_0)}{\rho_M(F)} \tag{2}$$

where $\rho(F_0)$ is the thermospheric density with normalized solar radiation F_0, $\rho(F)$ is the measured density with the observed solar radiation F, and ρ_M is the corresponding density obtained from the NRLMSISE-00 model.

In this study, the storm-time density enhancement is calculated with the difference between thermospheric density during geomagnetic storms and quiet time. Picone et al. (2002) showed that the NRLMSISE-00 model results underestimate the storm-time density, but they can simulate well with the observation in the quiet time. Since the CHAMP observations are relatively sparse from the previous quiet day, the quiet-time density from the NRLMSISE-00 model can be used as a reference to obtain density enhancement during geomagnetic storms.

2.2. Storm Classification

The thermospheric response can be variable with different magnitudes of geomagnetic storms (Wang, Miao, Aa, et al., 2020; Zesta & Oliveira, 2019). In this study, 265 geomagnetic storms are statistically analyzed from 2002 to 2008, and storm levels are classified by the minimum Dst values during storms (Gonzalez et al., 1999; Srivastava & Venkatakrishnan, 2004). The weak, moderate, and intense geomagnetic storms are based on the ranges of minimum Dst indices, -49 nT $<$ Dst ≤ -30 nT, -99 nT $<$ Dst ≤ -50 nT, and Dst ≤ -100 nT, respectively. The quiet time is defined as Dst > -30 nT for this statistical study.

Table 1 lists statistical geomagnetic storm cases from 2002 to 2008, identified for weak, moderate, and intense storms, respectively. The number (Num), date, and Day of Year (DOY) are also summarized for each storm. In this study, the 90% geomagnetic storms are used to assimilate the original NRLMSISE-00 model, so that the remaining 10% storms (not used to assimilate) can be kept to estimate and verify the calibrated NRLMSISE-00 model results. The 10% storms used to validate the calibration of the model are randomly chosen. Table 1 shows the 10% of the storms used for validation of the calibration results with asterisks (*), and the 90% of the storms for assimilation without asterisks. As a result, 123 weak, 103 moderate and 39 intense geomagnetic storms are explored for the statistics, while 111 weak, 103 moderate and 35 intense geomagnetic storms are used to assimilate the NRLMSISE-00 model, and 12 weak, 10 moderate and 4 intense storms can be used to test the calibration results.

2.3. Joule Heating

In this study, the distribution of height-integrated Joule heating is examined as the proxy for the major energy input (Deng et al., 2011; Thayer et al., 1995; Weimer, 2005). As mentioned in previous studies (Cai et al., 2016; Wang, Miao, Aa, et al., 2020; Wilson et al., 2006), the Joule heating ($\Sigma_p \boldsymbol{E}^2$) is calculated by height-integrated Pedersen conductance (Σ_p) and the electric field ($\boldsymbol{E}$).

The Pedersen conductance is mainly contributed by solar radiation and particle precipitation (Aksnes et al., 2002; Billett et al., 2018; Zhang et al., 2004). The height-integrated conductance has been derived from statistical patterns of particle precipitation based on the different magnitudes of geomagnetic storms (Hardy et al., 1987; Robinson et al., 1987):

$$\Sigma_{p(elec)} = \frac{40E_0}{16 + E_0^2}\sqrt{I}, \tag{3}$$

where E_0 and I are the average energy of particle precipitation and electron integral energy flux, obtained from the three satellites F16-F18 in Defense Meteorological Satellite Program (DMSP) spacecraft (Redmon et al., 2017). In this study, Pedersen conductance ($\Sigma_{p(elec)}$) can be calculated by particle precipitation with different AE index levels, 0 nT < AE ≤ 100 nT, 100 nT < AE ≤ 300 nT, 300 nT < AE ≤ 500 nT, 500 nT < AE ≤ 700 nT, 700 nT < AE ≤ 1000 nT, and AE ≥ 1000 nT. The conductance produced by solar radiation has been shown to be well represented as a function of the solar zenith angle, χ, the geomagnetic latitude, λ, and the 10.7 cm radio flux intensity, F10.7 (Rich et al., 1987), expressed as

$$\Sigma_{p(solar)} = \frac{12.5\sqrt{F10.7/180}\ \{0.06 + \exp[1.803\tanh(3.833\cos\chi) + 0.5\cos\chi - 2.332]\}}{\left[1 + 0.3\sin^2\lambda\right]\sqrt{1 - 0.99524\cos^2\lambda}}, \tag{4}$$

In addition, the electric field $\boldsymbol{E}$ is determined from the Weimer-2001 electric potential model (Weimer, 2001). The Weimer-2001 model includes the ionospheric electric potential from inputting Earth's dipole tilt, IMF, and solar wind conditions, and considers effects associated with nightside variations affected by geomagnetic substorms in the magnetotail. In this study, the Weimer, 2001 model is adopted with the input data from the Advanced Composition Explorer (ACE) satellite to calculate the ionospheric electric potential and the electric field.

Thus, the total Pedersen conductance can be calculated by adding $\Sigma_{p(solar)}$ and $\Sigma_{p(elec)}$ and times it with the electric field $\boldsymbol{E}$, the obtained distribution of height-integrated Joule heating (Σ_Q) can be expressed as

$$\Sigma_Q = \sqrt{\sum_{p(solar)}{}^2 + \sum_{p(elec)}{}^2}\boldsymbol{E}^2, \tag{5}$$

3. Results

In this section, the variations of Dst, AE, Joule heating, thermospheric density enhancement, and density discrepancy between the NRLMSISE-00 model and the observation are illustrated during the intense geomagnetic storm of November 20-21, 2003. In addition, 265 geomagnetic storms are statistically analyzed to show the overall presentation of storm-time thermospheric density response for this study.

Table 1
Geomagnetic Storm List

Num	Date	DOY	Num	Date	DOY	Num	Date	DOY	Num	Date	DOY
Weak Storms											
1	2002/01/25	25	2	2002/02/09	40	3	2002/03/03	62	4	2002/03/05	64
5	2002/03/19	78	6	2002/04/02	92	7	2002/04/13	103	8	2002/04/28	118
9	2002/05/21	141	10	2002/06/10	161	11	2002/07/06	187	12	2002/07/12	193
13*	2002/07/22	203	14	2002/07/27	208	15	2002/08/14	226	16	2002/08/26	238
17	2002/09/17	260	18	2002/09/22	265	19	2002/11/11	315	20	2002/11/13	317
21	2002/11/15	319	22	2002/12/01	335	23	2002/12/05	339	24	2002/12/07	341
25*	2002/12/14	348	26	2002/12/31	365	27	2003/01/19	19	28	2003/01/24	24
29	2003/02/06	37	30	2003/02/15	46	31	2003/03/06	65	32	2003/03/10	69
33	2003/03/14	73	34	2003/04/09	99	35	2003/04/14	104	36	2003/04/17	107
37*	2003/04/28	118	38	2003/05/07	127	39	2003/05/15	135	40	2003/06/14	165
41	2003/06/28	179	42	2003/08/01	213	43*	2003/08/28	240	44*	2003/09/04	247
45	2003/10/01	274	46	2003/10/24	217	47*	2003/11/09	313	48	2003/11/30	334
49	2003/12/14	348	50*	2004/01/01	01	51	2004/01/10	10	52*	2004/01/20	20
53	2004/02/03	34	54	2004/03/28	88	55	2004/04/16	107	56	2004/04/23	114
57	2004/04/30	121	58	2004/08/07	220	59	2004/08/22	235	60	2004/09/14	258
61	2004/09/17	261	62	2004/10/13	287	63	2004/10/20	394	64	2004/10/30	304
65	2004/11/17	322	66	2004/11/30	335	67	2004/12/11	346	68	2005/02/16	47
69	2005/03/18	77	70	2005/05/01	121	71	2005/05/13	133	72	2005/05/28	148
73	2005/06/05	156	74	2005/06/07	158	75	2005/06/17	168	76	2005/08/10	222
77	2005/08/29	241	78	2005/10/17	290	79	2005/10/25	298	80	2005/11/19	323
81	2005/12/27	361	82*	2006/02/20	51	83	2006/03/19	78	84	2006/03/21	80
85	2006/04/22	112	86	2006/05/04	124	87	2006/05/18	138	88	2006/06/06	157
89	2006/06/16	167	90	2006/07/05	186	91	2006/07/28	209	92	2006/08/07	219
93	2006/08/31	243	94	2006/09/04	247	95	2006/11/23	327	96	2007/01/17	17
97	2007/01/29	29	98	2007/02/14	45	99	2007/03/07	66	100*	2007/03/13	72
101	2007/03/25	84	102	2007/04/17	107	103	2007/04/28	118	104	2007/05/07	127
105	2007/07/15	196	106	2007/08/07	219	107	2007/09/06	249	108	2007/09/29	272
109*	2007/10/04	277	110	2007/11/22	326	111	2007/12/17	351	112	2008/01/13	13
113	2008/02/06	37	114*	2008/02/10	41	115	2008/02/15	46	116	2008/03/01	61
117	2008/03/26	86	118	2008/04/04	95	119	2008/04/16	107	120	2008/04/23	114
121	2008/06/15	167	122	2008/07/12	194	123	2008/09/15	259			
Moderate Storms											
1	2002/01/11	11	2	2002/02/02	33	3	2002/02/05	36	4	2002/03/01	60
5	2002/04/23	113	6	2002/05/15	135	7	2002/05/19	139	8	2002/05/27	147
9	2002/08/04	216	10	2002/09/11	254	11	2002/10/24	297	12	2002/10/27	300
13	2002/10/31	304	14	2002/11/18	322	15*	2002/11/20	324	16	2002/11/25	329
17	2002/12/19	353	18	2002/12/21	355	19	2002/12/23	357	20*	2002/12/27	361
21	2003/01/30	30	22	2003/02/02	33	23	2003/02/04	35	24	2003/02/27	58
25	2003/03/04	63	26	2003/03/16	75	27	2003/03/20	79	28	2003/03/27	86
29	2003/03/29	88	30	2003/03/31	90	31	2003/04/02	92	32	2003/04/04	94
33	2003/04/24	114	34	2003/05/01	121	35	2003/05/10	130	36*	2003/05/22	142
37	2003/06/02	153	38	2003/06/08	159	39	2003/06/21	172	40	2003/06/24	175

Table 1
Continued

Num	Date	DOY	Num	Date	DOY	Num	Date	DOY	Num	Date	DOY
41	2003/07/16	197	42*	2003/07/19	200	43	2003/07/27	208	44	2003/07/29	210
45	2003/08/06	218	46	2003/08/07	219	47	2003/08/21	233	48*	2003/09/17	260
49	2003/09/24	267	50	2003/10/14	287	51	2003/11/04	308	52	2003/11/11	315
53	2003/11/13	317	54	2003/12/06	340	55*	2003/12/10	344	56	2004/01/07	07
57	2004/01/15	15	58	2004/02/11	42	59	2004/03/11	71	60	2004/04/05	96
61	2004/07/17	199	62	2004/08/09	222	63	2004/11/25	330	64	2004/12/13	348
65	2005/01/01	01	66	2005/01/08	08	67	2005/01/12	12	68	2005/01/17	17
69	2005/02/07	38	70	2005/02/18	49	71	2005/03/07	66	72	2005/04/05	95
73	2005/05/20	140	74	2005/06/23	174	75	2005/07/10	191	76*	2005/07/18	199
77	2005/09/03	246	78	2005/09/04	247	79	2005/09/15	258	80	2005/10/08	281
81	2005/10/31	304	82	2005/12/11	345	83	2006/01/26	26	84*	2006/03/07	66
85	2006/04/05	95	86*	2006/04/09	99	87	2006/04/14	104	88	2006/05/06	126
89	2006/09/24	267	90	2006/10/01	274	91	2006/10/13	286	92	2006/11/10	314
93	2006/11/30	334	94	2006/12/06	340	95	2006/12/12	346	96	2007/04/01	91
97	2007/05/23	143	98	2007/10/25	298	99	2007/11/20	324	100	2008/02/28	59
101	2008/03/09	69	102	2008/09/04	248	103*	2008/10/11	285			
Intense Storms											
1	2002/03/24	83	2	2002/04/17	107	3	2002/04/18	108	4	2002/04/19	109
5	2002/04/20	110	6	2002/05/11	131	7*	2002/05/23	143	8	2002/08/02	214
9	2002/08/21	233	10	2002/09/04	247	11	2002/09/08	251	12	2002/10/01	274
13	2002/10/04	277	14	2002/10/07	280	15	2002/10/14	287	16*	2002/11/21	325
17	2003/05/29	149	18	2003/06/18	169	19	2003/07/12	193	20	2003/08/18	230
21	2003/10/30	303	22	2003/11/20	324	23	2004/01/22	22	24	2004/04/04	95
25	2004/07/23	205	26	2004/07/25	207	27	2004/07/27	209	28	2004/08/30	243
29	2004/11/08	313	30	2004/11/10	315	31	2005/01/18	18	32*	2005/05/08	128
33	2005/05/15	135	34*	2005/05/30	150	35	2005/06/13	164	36	2005/08/24	236
37	2005/08/31	243	38	2005/09/11	254	39	2006/12/15	349			

Note. * Shows the 10% of the storms used for validation of the calibration results with asterisks.

3.1. The November 20-21, 2003 Intense Geomagnetic Storm

The geomagnetic storm of November 20-21, 2003 is particularly intriguing, with AE and Dst up to 1698 nT and −422 nT. Figure 1 illustrates the temporal responses of thermospheric mass density from the CHAMP satellite and NRLMSISE-00 model during this intense storm. Figure 1a–1d show Dst index, AE index, the time series of total integrated Joule heating for the northern hemisphere (blue) and southern hemisphere (red), thermospheric density from CHAMP (blue), NRLMSISE-00 (red), and in the quiet time as the reference (black). The density in the quiet time is obtained from the NRLMSISE-00 with the Ap index on 19 November 2003 (the day before this storm).

From geomagnetic activity indices in Figure 1a and 1b, it can be found that Dst sharply decreases at 13 hr and reaches the peak at 21 hr, while AE index increases to its maximum/peak at 17 hr, ahead of Dst for 4 hr. Both northern and southern hemispheres Joule heating increase at 7 h and reach their peaks at 16 hr. Joule heating in the southern hemisphere is stronger than that in the northern hemisphere, which indicates more electromagnetic energy entering the southern hemisphere thermosphere during the geomagnetic storm. As for thermospheric density, both observation and simulation increase to the maximum at about 20 hr, lagging AE, Joule heating for 3

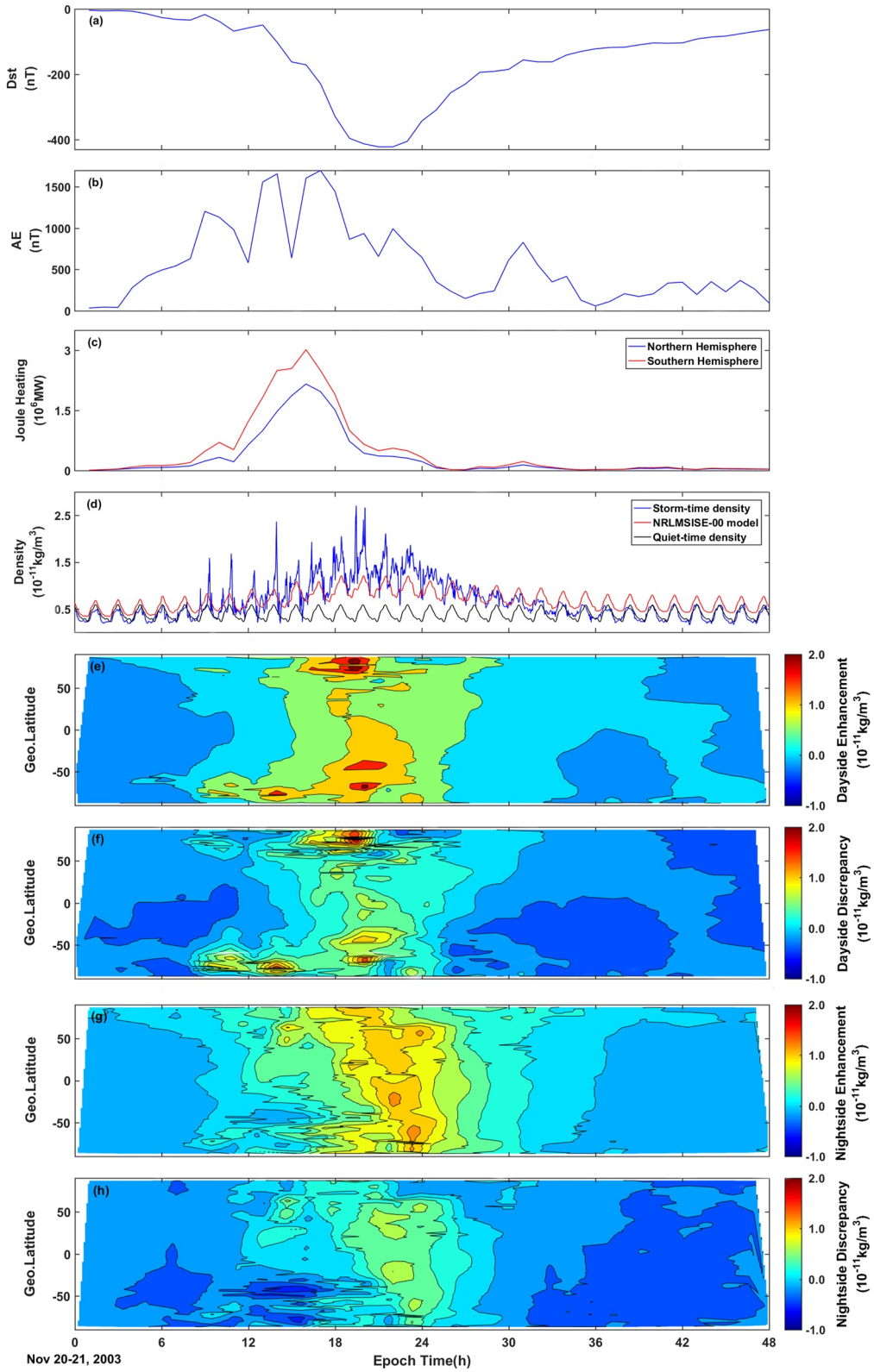
(a)
Dst (nT)
0
-200
-400
(b)
AE (nT)
1500
1000
500
0
(c)
Joule Heating (10^6MW)
3
1.5
0
Northern Hemisphere
Southern Hemisphere
(d)
Density (10^{-11}kg/m^3)
2.5
1.5
0.5
Storm-time density
NRLMSISE-00 model
Quiet-time density
(e)
Geo.Latitude
50
0
-50
Dayside Enhancement (10^{-11}kg/m^3)
2.0
1.0
0.0
-1.0
(f)
Geo.Latitude
Dayside Discrepancy (10^{-11}kg/m^3)
(g)
Geo.Latitude
Nightside Enhancement (10^{-11}kg/m^3)
(h)
Geo.Latitude
Nightside Discrepancy (10^{-11}kg/m^3)
0
6
12
18
24
30
36
42
48
Nov 20-21, 2003
Epoch Time(h)

Figure 1.

and 4 hr, and peaking 1 hr earlier than Dst. In general, the NRLMSISE-00 simulates well for density observation, but vastly underestimates the density peaks during the geomagnetic storm.

Figures 1e–1h depict the density enhancement and density discrepancy versus epoch time and geographic latitude (GLAT) on the dayside and nightside, respectively. The density enhancement represents the difference between the storm-time and the quiet-time density, and density discrepancy refers to the difference between the observation and model simulation. On the dayside, the density enhancement increases at about 9h at 70°S, which indicates that the storm-time density is more strongly affected by strengthened Joule heating input at about 7h in the southern hemisphere. The time lag of thermospheric density to Joule heating can result from the different heights of density and Joule heating. In this study, the thermospheric density is explored at 400 km, and Joule heating deposits at lower altitudes as geomagnetic activity intensifies (Cheng et al., 2017; Wu et al., 2020). Thus, Joule heating needs time to conduct upward to affect the density at 400 km (Huang et al., 2012; Wang, Miao, Aa, et al., 2020).

The dayside thermospheric density enhancement reaches the peak, 2.0×10^{-11} kg/m^3, at about 20hr in the cusp region 60°N–80°N and 60°S, where the density discrepancy reaches the maximum of about 1.4×10^{-11} kg/m^3 at the same time. The density enhancement and discrepancy at high latitudes reach the peaks in both hemispheres around the main phase of the storm. At the middle and low latitudes, the density in the southern hemisphere is larger than in the northern one. In addition, the nightside density enhancement increases up to 1.0×10^{-11} kg/m^3 at 20°S–30°S and 60°S–70°S much smaller than that on the dayside. It can also be found that the density discrepancy peaks larger on the dayside (1.4×10^{-11} kg/m^3) as compared to the nightside (0.8×10^{-11} kg/m^3). As a result, during the geomagnetic storm, the model underestimates thermospheric density, especially the storm-time density peaks (model density peaks up to 1.3×10^{-11} kg/m^3 and observed density peaks up to 2.7×10^{-11} kg/m^3).

Due to the limitation of measurement availability by satellites, both CHAMP and GRACE satellites can be used to increase the spatial coverage to estimate the global response of storm-time thermospheric density as much as possible. By assuming that the density changes between successive orbits are progressive, the linear interpolated densities are used to capture the storm-time peak values, which can partially reflect the global response. Figure 2 shows the temporal and spatial Northern Hemispheric distribution of thermospheric density and Joule heating per 3h from 1200UT to 2400UT on 20 November 2003, intense geomagnetic storm. The areas with blank represent that the density observations are very sparse and linear interpolation fails to fill up the gaps.

During the geomagnetic storm, the thermospheric density increases at high latitudes at 60°N–80°N, at 1500–1800UT (Figure 2b), then the density peaks at 1800–2100UT in the cusp region with 65°N-80°N (Figure 2c), which has also seen in Figure 1e. The NRLMSISE-00 model vastly underestimates the storm-time observation in the cusp region, especially to the density peaks (Figure 2g). Joule heating peaks at high latitude at 50°N–60°N, at 1200–1500UT (Figure 2i), and then it increases in the middle latitudes at 1500–1800UT (Figure 2j). It can also be found that the thermospheric density delays Joule heating during the geomagnetic storm.

3.2. Statistics for Time Difference

As shown in the storm event during November 20-21, 2003, it has been found that the thermospheric density peaks earlier than maximum values of Dst, and later than AE and Joule heating. To investigate the responses of thermospheric density to Dst and AE, the time differences between the peak thermospheric densities and Dst indices, and between peak densities and AE indices are statistically examined from 265 geomagnetic storms as shown in Figure 3. Figures 3a, 3c, and 3e show that the time differences between peak density and Dst are mainly concentrated on the negative during geomagnetic storms, which indicates that the Dst indices lag the storm-time thermospheric densities. As shown in Figures 3a and 3c, 55% of weak geomagnetic storms and 46% of moderate storms involve thermospheric density peaking within the combined ranges of $-0.5 \sim 0.5$ hr and $0.5 \sim 1.5$ hr before Dst, while it peaks within the ranges from $-0.5 \sim 0.5$ hr to $1.5 \sim 2.5$ hr for 67% intense geomagnetic

Figure 1. The temporal variations of different parameters under the intense geomagnetic storm event on November 20-21, 2003. (a) Dst index, (b) AE index, (c) total integrated Joule heating for northern (blue line) and southern hemisphere (red line), (d) thermospheric density observed from the CHAMP satellite (blue line) measurement, NRLMSISE-00 model (red line) simulation, compared with the prediction of the NRLMSISE-00 in the quiet time (black line), (e) density enhancement (storm time – quiet time) and (f) density discrepancy (observation – simulation) on the dayside, (g) density enhancement on the nightside and (h) density discrepancy on the nightside.

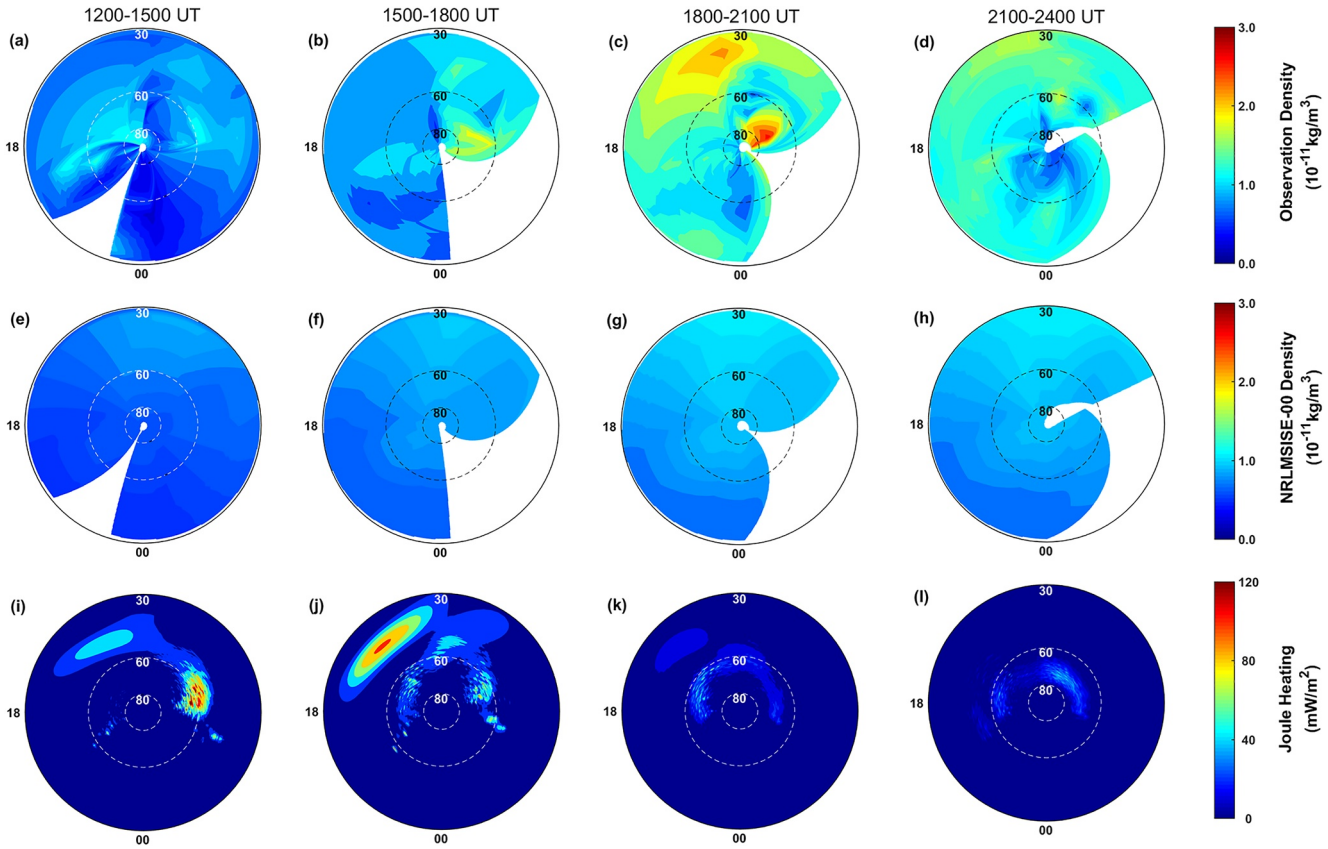

Figure 2. Intense geomagnetic storm event of 20 November 2003. (a–d) Thermospheric density observation, (e–h) NRLMSISE-00 model density, and (i–l) height-integrated Joule heating during 20 November 2003, at 1200UT–1500UT, 1500–1800UT, 1800–2100UT, and 2100–2400UT, respectively. The patterns are plotted in latitude versus local time coordinates, with the center corresponding to the North Pole.

storms in Figure 3e. In general, Dst lags thermospheric density for about 1 hr during geomagnetic storms, while the lag times are more concentrated at longer times as storms intensify.

Figures 3b, 3d, and 3f depict the time differences between the peak densities and AE indices for weak, moderate, and intense geomagnetic storms. During weak geomagnetic storms (Figure 3b), 57% of the cases involve thermospheric densities peaking within the combined ranges of $-0.5 \sim 0.5$ hr and $0.5 \sim 1.5$ hr after AE indices, while it peaks within the ranges from $-0.5 \sim 0.5$ hr to $1.5 \sim 2.5$ hr for 63% of moderate storms (Figure 3d). In Figure 3f, 61% of intense geomagnetic storms involve the peak density lagging AE within the ranges from 1.5–2.5 hr to $3.5 \sim 4.5$ hr, which is longer than that for weak and moderate storms. As storm intensity increases, the lag time of density to AE increases.

AE and Dst indices represent the geomagnetic activity in the high latitude regions and equatorial regions. To explore the relation between high-latitude and low-latitude geomagnetic activity, the time difference between Dst and AE is calculated for weak, moderate, and intense storms in Figure 4a, 4c, and 4e. During weak geomagnetic storms, Dst delays AE within the range of $0.5 \sim 1.5$ hr, while it is concentrated on the combined ranges of $0.5 \sim 1.5$ hr and $1.5 \sim 2.5$ hr for moderate storms. For intense geomagnetic storms, the lag time of Dst to AE ranges from 2.5–3.5 hr to $4.5 \sim 5.5$ hr. In general, Dst lags AE for a longer time as storm intensity increases. This implies that the high latitudes have an initial effect on geomagnetic storms, then the middle-low latitude regions respond, and such lag time extends as storms intensify.

The time difference between the peaks in thermospheric density and Joule heating is also demonstrated in Figure 4b, 4d and 4f during geomagnetic storms. As shown in Figure 4b, the peak thermospheric density follows Joule heating within the combined ranges of $-0.5 \sim 0.5$ hr and $0.5 \sim 1.5$ hr later during weak geomagnetic storms.

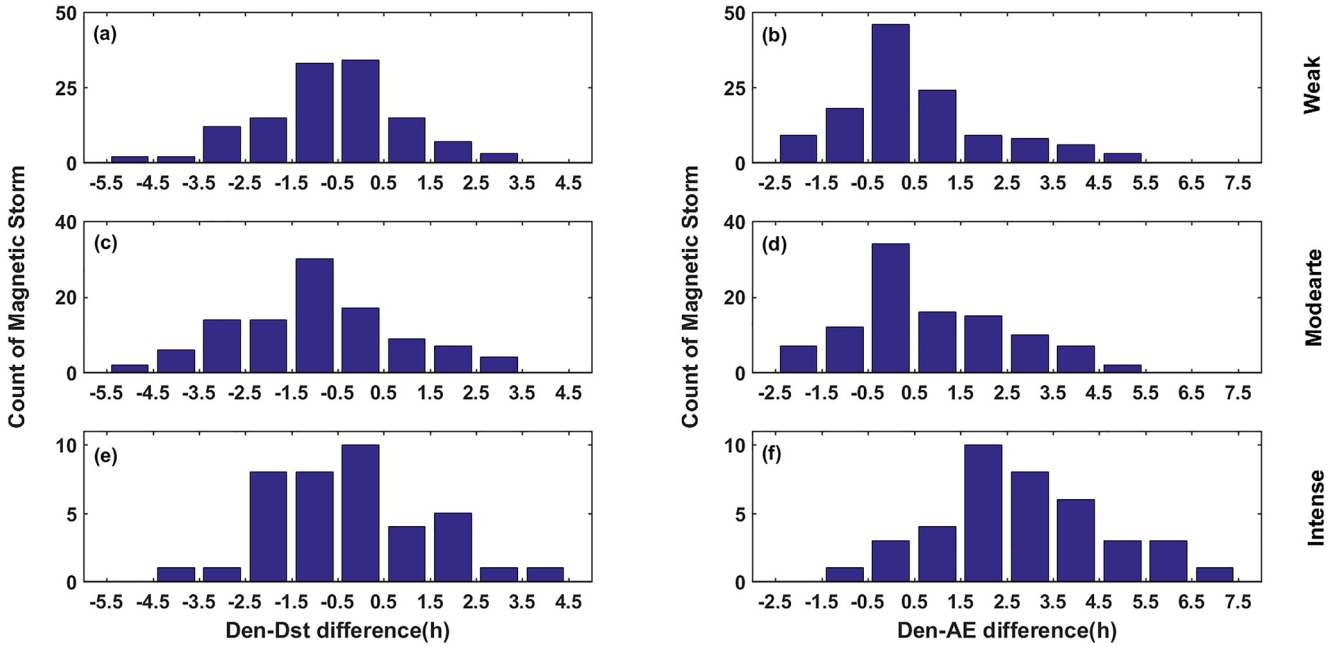

Figure 3. (Left column) Time difference between thermospheric density peak and Dst peak, and (right column) between peak density and peak AE during (a) & (b) weak, (c) & (d) moderate, and (e) & (f) intense geomagnetic storms from 265 geomagnetic storm cases. Positive time differences mean that thermospheric density lags a longer time than Dst and AE indices.

Figure 4d shows that moderate storms involve peak density lagging Joule heating within the combined ranges of 0.5 ~ 1.5 hr and 1.5 ~ 2.5 hr, while it ranges from 2.5–3.5 hr to 4.5 ~ 5.5 hr for intense geomagnetic storms in Figure 4f. In other words, thermospheric density has a longer lag time behind Joule heating as storms intensify.

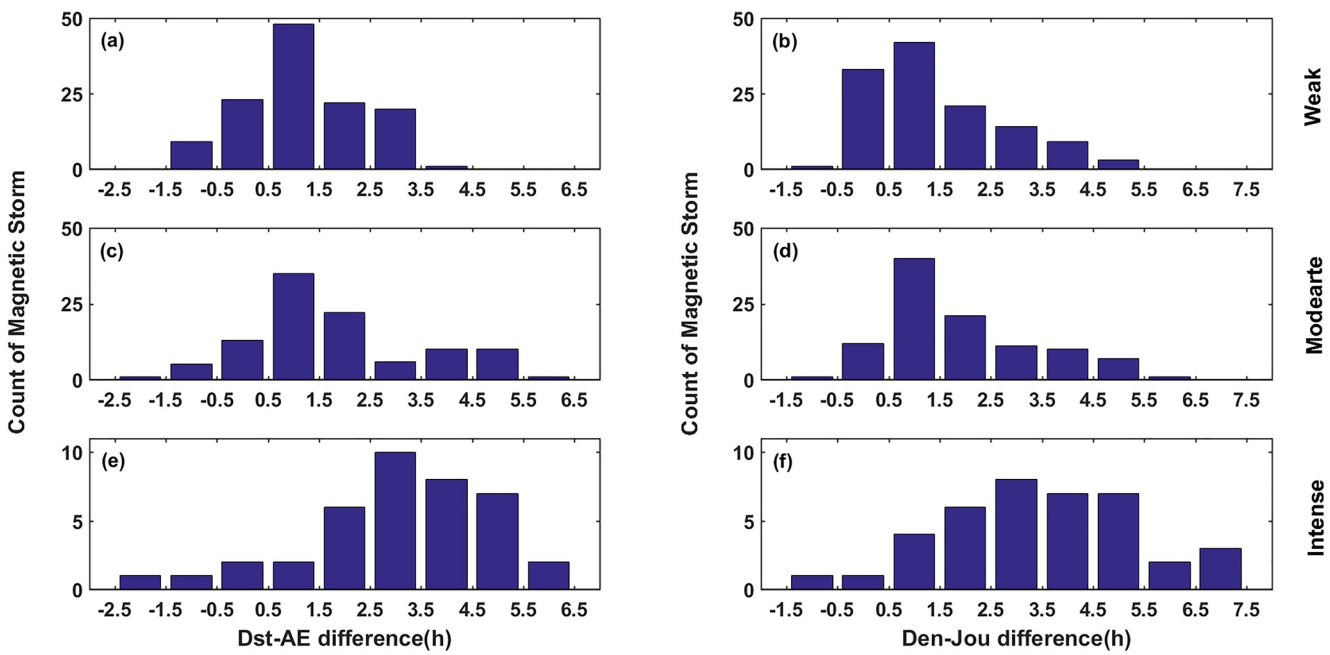

Figure 4. (Left column) Time difference between peak Dst and peak AE, and (right column) between peak thermospheric density and peak Joule heating during (a) & (b) weak, (c) & (d) moderate, and (e) & (f) intense geomagnetic storms from 265 geomagnetic storm cases. Positive time differences mean that Dst indices lag AE indices, and thermospheric density lags a longer time than Joule heating.

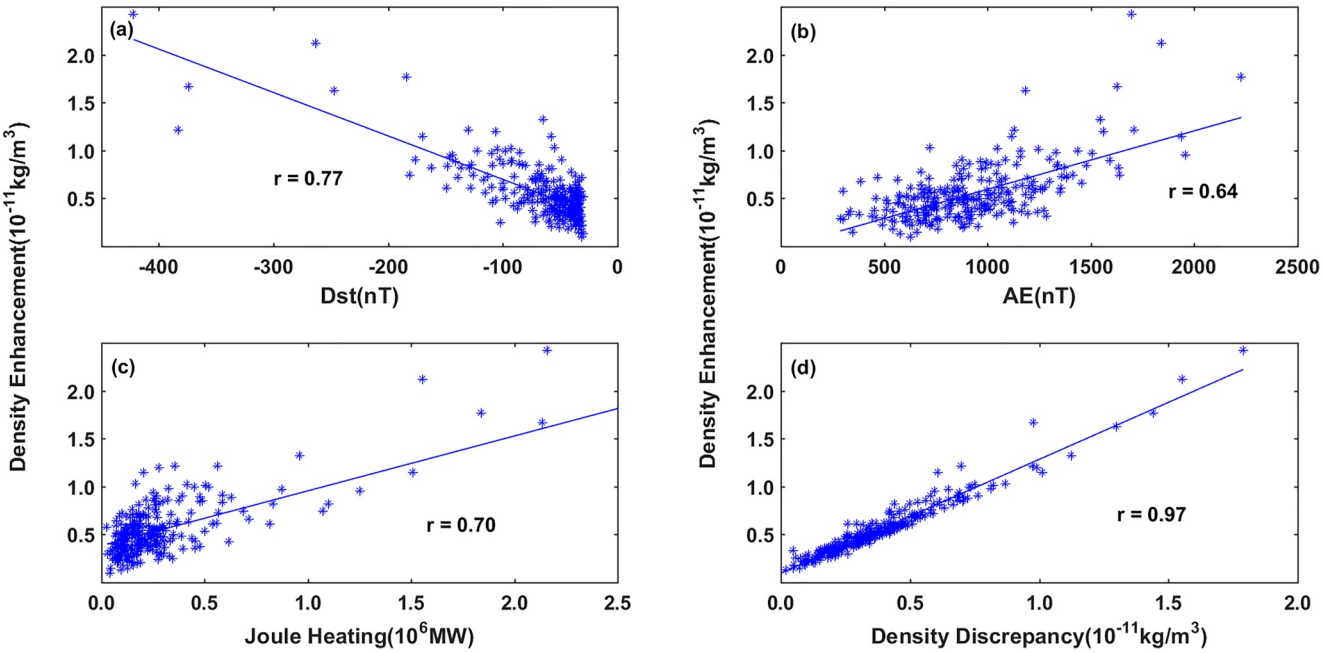

Figure 5. Distribution of peak thermospheric density enhancement and (a) Dst, (b) AE, (c) peak Joule heating, and (d) peak density discrepancy from 265 geomagnetic storms cases. The blue line is the fitting line during storms.

3.3. Statistics for Correlation

During the intense geomagnetic storm on November 20-21, 2003, thermospheric density enhancement varies with Dst, AE, and Joule heating, while the density discrepancy between observation and model increases due to the model underestimating the storm-time density enhancement. In Figure 5, 265 geomagnetic storms are statistically analyzed to show the scatterplot and linear regression of peak density enhancement with Dst, AE, peak Joule heating, and peak density discrepancy, during geomagnetic storms. Figures 5–5c show that peak thermospheric density enhancement increases with decreasing Dst, increasing AE, and peak Joule heating as geomagnetic storms intensify. The correlation coefficients (r) of density enhancement with Dst (0.77), AE (0.64), and Joule heating (0.70) are also calculated. In Figure 5d, it can be noted that the peak density discrepancy increases with the peak density enhancement, while the correlation coefficient between density discrepancy and density enhancement is 0.97. This indicates that the NRLMSISE-00 model underestimates the impact of geomagnetic storms on the thermospheric density enhancement, especially to the storm-time peak density.

4. Assimilation for Calibrating NRLMSISE-00

As shown in Figures 5a–5c, density enhancement has a quasi-linear relationship with Dst, AE, and Joule heating during geomagnetic storms. Dst, AE, and Joule heating can be used to roughly fit the quantitative functional relation of density enhancement. In addition, the density discrepancy correlates well with the density enhancement in Figure 5d. Thus, the relationship between density discrepancy and density enhancement can also be used to fit the functional relation of density discrepancy. As a result, based on the functional relation of density enhancement with Dst, AE, Joule heating, and density discrepancy, the assimilation for density discrepancy can be established as follows:

$$\begin{cases} Density\,enhancement_{t0} = a + b \times JH_{t1} + c \times Dst_{t2} + d \times AE_{t3} \\ Density\,discrepancy_{t0} = e \times Density\,enhancement_{t0} + f \end{cases}, \tag{6}$$

where JH, Dst, and AE are Joule heating, Dst, and AE indices during geomagnetic storms. The coefficients, a, b, c, and d are based on the relationship of density enhancement with Dst, AE, and Joule heating, while e and f are

calculated from the relation between density discrepancy and density enhancement. In addition, t0, t1, t2, and t3 are the peak times for density enhancement/density discrepancy, Joule heating, Dst, and AE. The response times of thermospheric density to geomagnetic activity indices (AE and Dst) and Joule heating vary as storms intensify. Based on the statistical conclusion of the time difference in Section 3.2, the relationship of t0 with t1, t2, and t3 can also be displayed during weak, moderate, and intense geomagnetic storms, respectively:

$$\begin{cases} t1 = t0 - 1 \\ t2 = t0 + 1, \\ t3 = t0 \end{cases} \begin{cases} t1 = t0 - 2 \\ t2 = t0 + 1, \\ t3 = t0 \end{cases} \begin{cases} t1 = t0 - 4 \\ t2 = t0 + 1, \\ t3 = t0 - 3 \end{cases} \tag{7}$$

In this study, 123, 103, and 39 geomagnetic storm cases are statistically explored for weak, moderate, and intense storms, respectively. 90% of the storm cases (111 weak, 103 moderate, and 35 intense geomagnetic storms) are used to calculate the coefficients (a, b, c, d, e, and f) fitted in functional Equation (6) and set up Equations (8–10) for weak, moderate and intense storms. The remaining 10% storms (not used to assimilate) including 12 weak, 10 moderate, and 4 intense storms are used to test the calibration results. Based on the 90% geomagnetic storms, the calibration of NRLMSISE-00 for different magnitudes storms can be respectively expressed by

$$\begin{cases} EDE_t = 1.7962 \times 10^{-12} + 3.3707 \times 10^{-18} \times JH_{t-1} - 3.4610 \times 10^{-14} \times Dst_{t+1} + 5.9681 \times 10^{-16} \times AE_t \\ EDD_t = 0.9445 \times EDE_t - 1.0299 \times 10^{-12}, \end{cases} \tag{8}$$

$$\begin{cases} EDE_t = 7.6770 \times 10^{-13} + 3.8214 \times 10^{-18} \times JH_{t-2} - 4.4014 \times 10^{-14} \times Dst_{t+1} + 1.0480 \times 10^{-15} \times AE_t \\ EDD_t = 0.9265 \times EDE_t - 1.2428 \times 10^{-12}, \end{cases} \tag{9}$$

$$\begin{cases} EDE_t = -2.5056 \times 10^{-13} + 1.7376 \times 10^{-18} \times JH_{t-4} - 2.7710 \times 10^{-14} \times Dst_{t+1} + 3.0305 \times 10^{-15} \times AE_{t-3} \\ EDD_t = 0.7879 \times EDE_t - 9.7010 \times 10^{-13}, \end{cases} \tag{10}$$

where EDE is the Estimated Density Enhancement, EDD is Estimated Density Discrepancy between in-situ observed density and original NRLMSISE-00 model. JH, Dst, and AE are Joule heating, Dst, and AE indices during geomagnetic storms. In this study, Joule heating, Dst, and AE from 90% of geomagnetic storms are used to fit the functional relations in Equations (8–10) for calibrating the original model. During a geomagnetic storm, the Joule heating, Dst, and AE can be obtained to calculate the EDD, as the storm-time calibration factor for the NRLMISIE-00 model. As a result, the sum of both the original NRLMSISE-00 and the EDD is calculated as the calibration results of NRLMSISE-00.

5. Verification

5.1. Assimilation (90% Storms) and Validation (10% Storms)

Based on the 90% of geomagnetic storms to fit the functional relation, the calibration of storm-time NRLMSISE-00 assimilated in Equations (8–10) can be used to correct the simulation of storm-time thermospheric density. To test the simulation results of calibrated NRLMSISE-00 model during geomagnetic storms, the calibration of NRLMSISE-00 for assimilation results with 90% of the storms and the validation with 10% of the storms are illustrated in Figure 6. Figure 6 depicts the peaks of calibrated NRLMSISE-00 (blue), observed thermospheric densities (red), and original NRLMSISE-00 densities (black) during weak (a), moderate (b), and intense (c) storms. The assimilation is on the left of Figure 6 with white background, while the validation is shown on the right with green background.

During weak geomagnetic storms (Figure 6a), the observed density ranges from 0.4×10^{-11} kg/m^3 to 1.3×10^{-11} kg/m^3, while the original model ranges from 0.2×10^{-11} kg/m^3 to 0.7×10^{-11} kg/m^3. The observed

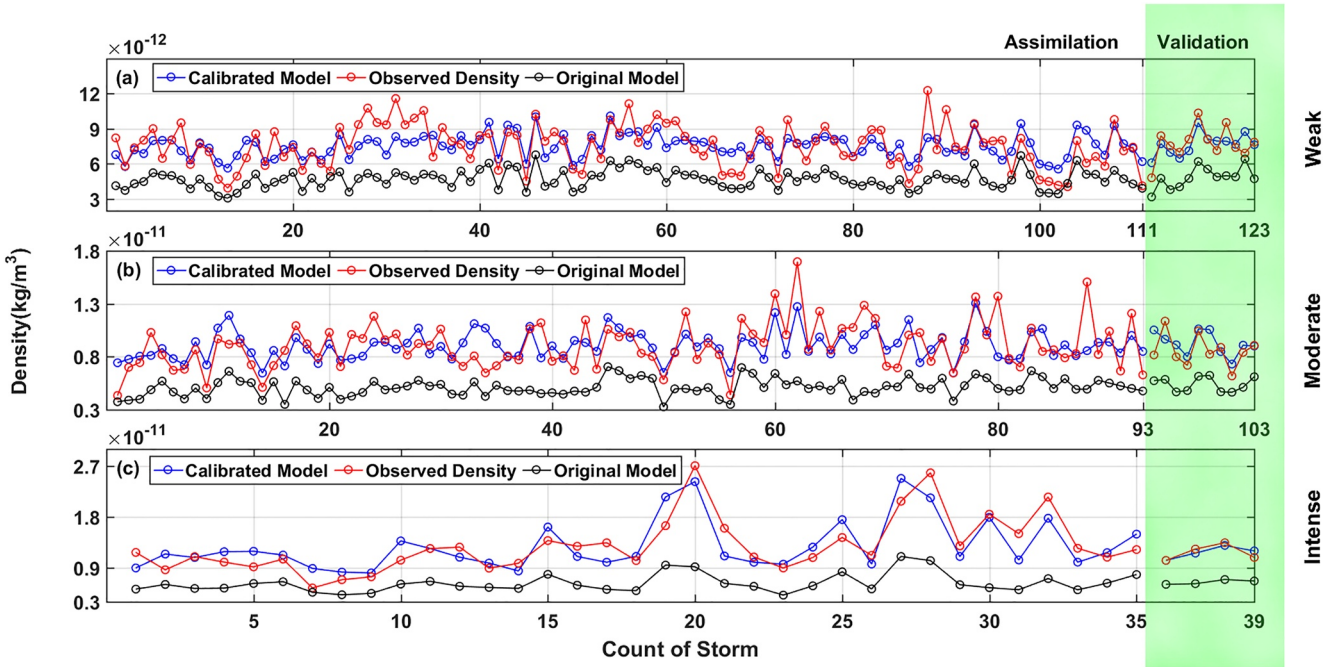

Figure 6. The calibrated density (blue line), the observed density (red line), and the density from original NRLMSISE-00 (black line) during (a) weak, (b) moderate, and (c) intense geomagnetic storms. The density with white background is the assimilation on the left of the Figure and the validation is shown on the right with green background.

densities peak vastly larger than NRLMSISE-00. However, the calibrated NRLMSISE-00 ranges from 0.5×10^{-11} kg/m^3 to 1.1×10^{-11} kg/m^3, fluctuating around the peak density observations. During moderate (Figure 6b) and intense (Figure 6c) geomagnetic storms, the observation ranges from 0.4×10^{-11} kg/m^3 to 1.7×10^{-11} kg/m^3 and 0.7×10^{-11} kg/m^3 to 2.7×10^{-11} kg/m^3, while the model ranges from 0.3×10^{-11} kg/m^3 to 0.8×10^{-11} kg/m^3 and 0.3×10^{-11} kg/m^3 to 1.0×10^{-11}. The NRLMSISE-00 model underestimates the peak observed density, but the calibration result simulates well, ranging from 0.6×10^{-11} kg/m^3 to 1.3×10^{-11} kg/m^3 and 0.9×10^{-11} kg/m^3 to 2.6×10^{-11} kg/m^3. In general, the calibration results simulate thermospheric density better than the NRLMSISE-00 model.

The Mean Relative Error (MRE $= \frac{observation-model}{observation}$) is also calculated and determined by the percentage between the observation-model difference and the observation for assimilation and validation during geomagnetic storms. During weak and moderate geomagnetic storms, MRE between the observed density (red line) and original model (black line) is about 35% (Figure 6a) and 40% (Figure 6b), while that for intense storms is 45% (Figure 6c). This indicates that the density discrepancy can increase as storms intensify. The MRE of the assimilation (red line and blue line on the left) is mostly between 10% and 15% for weak (Figure 6a) and moderate (Figure 6b) storms, while it is about 10% during intense storms (Figure 6c). For validation (red line and blue line on the right with green background), the MRE is about 10% for weak (Figure 6a), moderate (Figure 6b), and intense (Figure 6c) geomagnetic storms. In general, the MRE of the original model is about 40%, while after calibration it decreases to 10% during geomagnetic storms. Both assimilation and validation results can prove that the calibrated model results have a better agreement than the original model during geomagnetic storms.

5.2. Calibration of the November 20-21, 2003 Intense Geomagnetic Storm With GRACE Satellite

As outlined in Section 3.1, the NRLMSISE-00 underestimated the observed thermospheric density, and the density discrepancy increased with density enhancement for an intense geomagnetic storm. According to variation of Dst during November 20-21, 2003, Equations (8–10) can be used to correct the original model and the validation of the calibration is verified with the GRACE satellite. Figure 7 depicts the variation of thermospheric density on November 20-21, 2003. The top row shows GRACE observed density on the dayside and nightside,

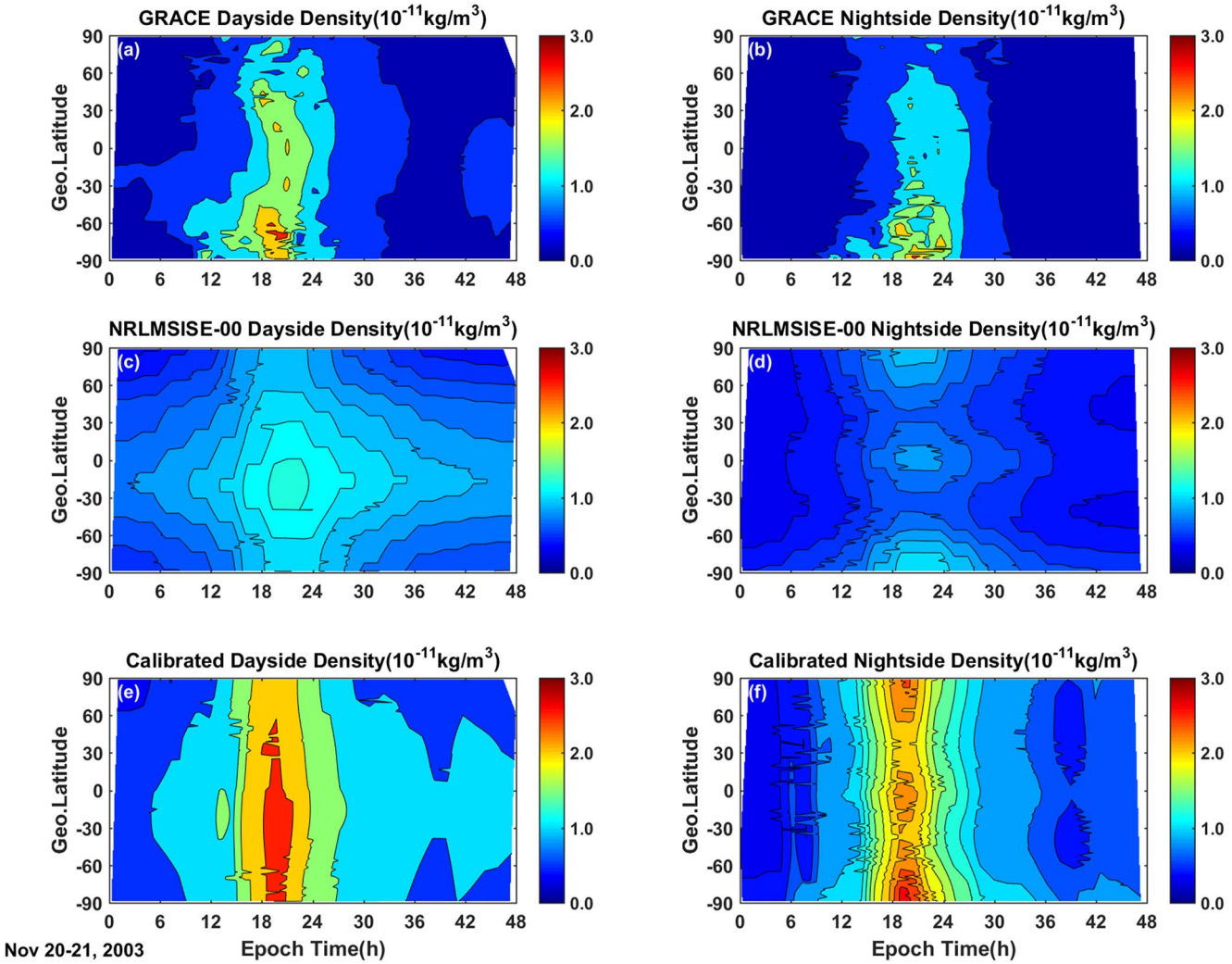

Figure 7. Intense geomagnetic storm event of November 20-21, 2003. (Left column) Dayside density and (right column) nightside density from (a) & (b) Gravity Recovery and Climate Experiment satellite, (c) & (d) the original NRLMSISE-00 model, and (e) & (f) the calibrated model.

respectively, and the middle and bottom rows show the corresponding densities simulated by the original NRLMSISE-00 model and calibrated model.

On the dayside, Figure 7a shows that dayside thermospheric density increases at 9h at about 60°S, peaking about 2.7×10^{-11} kg/m^3 at 20hr in the cusp region at 60°S–75°S, and the nightside observed density increases to the peak about 2.5×10^{-11} kg/m^3 at 85°S in Figure 7b. The cusp region is well-known for thermospheric density enhancements in the high-latitude thermosphere during geomagnetic storms (Kwak et al., 2009; Lühr et al., 2004; Wang et al., 2021). However, the original NRLMSISE-00 model vastly underestimates GRACE density observations in the cusp region, especially to the density peaks (Figures 7c and 7d). Billett et al. (2021) revealed the impact of solar-terrestrial energy on thermosphere, such as Poynting flux (PF) mainly depositing in the cusp regions. Even more, Knipp et al. (2021) concluded that Poynting flux in the cusp region often exceeds the energy intensity in the auroral zone. The NRLMSISE-00 model simulating observed density may underestimate energy deposition at high latitudes during geomagnetic storms.

After combining the dominated energy during storms, Joule heating, and geomagnetic activity indices, the calibrated NRLMSISE-00 can better reflect the storm-time density in Figures 7e and 7f. The dayside calibration increases to the peaks, 2.7×10^{-11} kg/m^3 at about 20hr at regions of 40°N-90°S, while it is wider than the observed density peak (Figure 7a). Figure 7f illustrates that calibrated model peaks at about 20hr at 75°S–85°S at about 2.5×10^{-11} kg/m^3, slightly wider than the peak density observed in the nightside (Figure 7b). The original

model underestimates the equatorial density, while the calibrated model overestimates the thermospheric density at low latitudes.

According to previous studies, during the geomagnetic storm, solar wind brings tremendous energy into the magnetosphere-ionosphere-thermosphere system at high latitudes (Buonsanto, 1999; Sutton et al., 2009), heating the thermospheric density to increase (Wilson et al., 2006). Due to the large-scale gravity waves and wind surges, the density will also increase at low latitudes and equator (Emmert, 2015; Fuller-Rowell et al., 1994, 2013). The calibration of the model was calculated with the influence of Joule heating on density, while the gravity waves and neutral winds are not considered for density variation at the equator. Thus, the calibration model results for the equatorial density may be overestimated. In general, although the calibration has some errors to reflect the storm-time density variation, the simulation results of calibrated NRLMSISE-00 can reproduce the GRACE observation better than the original.

6. Summary and Discussion

In this study, the relationships of thermospheric density with geomagnetic activity indices and Joule heating during geomagnetic storms were investigated for a period from 2002 to 2008, and employed to calibrate the thermospheric model NRLMSISE-00. First, during moderate and weak storms, the response time of thermospheric density to AE indices is around 0–1 hr, while during intense storms it is about 2–4 hr. Second, Dst indices delay thermospheric densities for about 1 hr during storms. Third, the peak Dst indices delay the peak AE indices during geomagnetic storms. The time difference between Dst and AE is approximately 1–2 hr for weak and moderate storms, while it is about 3–5 hr for intense storms. Finally, the calibration of the NRLMSISE-00 model is established by the function of time differences and quasi-linear correlations between thermospheric density and geomagnetic activity indices, and between density and Joule heating. It can also be found that the calibration can improve the accuracy of simulation with MRE of 10%, better than the original model with MRE of 40%.

The high-latitude geomagnetic activity indices AE shows the changes in auroral electrojet, the difference between eastward electrojet (AU) and westward electrojet (AL), and the low-latitude geomagnetic activity indices Dst illustrates the variation of the equatorial ring current. Rostoker et al. (1980) found that the auroral electrojet varies with enhanced field-aligned currents (FACs) and particle precipitation in the nightside auroral region. This variation process of auroral electrojet is transient and takes short time to respond. The ring current increases with the injection of massive ions and electrons from the magnetotail to the inner magnetosphere, leading to global magnetic disturbance (Gonzalez et al., 1994). The magnetospheric perturbations associated with large-scale and strong variation need a longer time to transfer energy. In addition, Maggiolo et al. (2017) also found that the AE indices respond to the interplanetary magnetic field (IMF) Bz regarding shorter response time than the horizontal geomagnetic field (SYM-H) indices, which is used instead of Dst indices with higher time resolution. As a result, the low-latitude geomagnetic activity indices Dst can lag the high-latitude geomagnetic activity indices AE for a while.

Please note that the peak density enhancement and peak density discrepancy were used as proxies for every geomagnetic storm when the NRLMSISE-00 model discrepancies were explored. These discrepancies would represent the extreme cases (likely the largest errors) for the model to underestimate the densities during storms. Therefore, based on our results sampling the peak (extreme) values for the particular storms to establish the calibrated function, the calibration of the NRLMSISE-00 model may slightly overestimate the density observations in other times when the density responses are moderate (not the peaks). In addition, it is not considered the impact on equatorial density during geomagnetic storms, such as neutral winds and gravity waves. The calibrated model may overestimate the density observations at low latitude regions. Further study will take low-latitude influences on thermospheric density into account to calibrate the NRLMSISE-00 model, such as neutral winds and gravity waves.

Data Availability Statement

The CHAMP and GRACE neutral mass density is obtained from http://thermosphere.tudelft.nl/. The geomagnetic activity indices Dst and AE are obtained from http://wdc.kugi.kyoto-u.ac.jp/. The DMSP data and ACE data are obtained from https://cdaweb.gsfc.nasa.gov/index.html/ and https://omniweb.gsfc.nasa.gov/. The solar

radiation proxy F10.7 is obtained from https://omniweb.gsfc.nasa.gov/form/dx1.html. The NRLMSISE-00 and Weimer model are from https://ccmc.gsfc.nasa.gov/.

Acknowledgments
This work is supported by the Key Research Program of the Chinese Academy of Sciences, Grant Nos. ZDRE-KT-2021-3 and the National Science Foundation of China (41674183 and 41974184).

References

Adebesin, B. O. (2016). Investigation into the linear relationship between the AE, Dst and ap indices during different magnetic and solar activity conditions. *Acta Geodaetica et Geophysica*, *51*(2), 315–331. https://doi.org/10.1007/s40328-015-0128-2

Aikio, A. T., Cai, L., & Nygrén, T. (2012). Statistical distribution of height-integrated energy exchange rates in the ionosphere. *Journal of Geophysical Research*, *117*(A10), A10325. https://doi.org/10.1029/2012JA018078

Aikio, A. T., & Selkälä, A. (2009). Statistical properties of Joule heating rate, electric field and conductances at high latitudes. *Annals of Geophysics*, *27*(7), 2661–2673. https://doi.org/10.5194/angeo-27-2661-2009

Aksnes, A., Stadsnes, J., Bjordal, J., Tgaard, N., Vondrak, R. R., Detrick, D. L., et al. (2002). Instantaneous ionospheric global conductance maps during an isolated substorm. *Annals of Geophysics*, *20*(8), 1181–1191. https://doi.org/10.5194/angeo-20-1181-2002

Billett, D. D., Grocott, A., Wild, J. A., Walach, M. T., & Kosch, M. J. (2018). Diurnal variations in global joule heating morphology and magnitude due to neutral winds. *Journal of Geophysical Research: Space Physics*. https://doi.org/10.1002/2017ja025141

Billett, D. D., Perry, G. W., Clausen, L. B. N., Archer, W. E., McWilliams, K. A., Haaland, S., et al. (2021). The relationship between large scale thermospheric density enhancements and the spatial distribution of Poynting flux. *Journal of Geophysical Research: Space Physics*, *126*(5), e2021JA029205. https://doi.org/10.1029/2021JA029205

Bruinsma, S., Forbes, J. M., Nerem, R. S., & Zhang, X. (2006). Thermosphere density response to the 20–21 November 2003 solar and geomagnetic storm from CHAMP and GRACE accelerometer data. *Journal of Geophysical Research*, *111*(A6), A06303. https://doi.org/10.1029/2005JA011284

Bruinsma, S., Tamagnan, D., & Biancale, R. (2004). Atmospheric densities derived from CHAMP/STAR accelerometer observations. *Planetary and Space Science*, *52*(4), 297–312. https://doi.org/10.1016/j.pss.2003.11.004

Buonsanto, M. J. (1999). Ionospheric storms—A review. *Space Science Reviews*, *88*(3/4), 563–601. https://doi.org/10.1023/A:1005107532631

Cai, L., Aikio, A. T., & Milan, S. E. (2016). Joule heating hot spot at high latitudes in the afternoon sector. *Journal of Geophysical Research: Space Physics*, *121*(7), 7135–7152. https://doi.org/10.1002/2016JA022432

Cai, L., Aikio, A. T., & Nygrén, T. (2013). Height-dependent energy exchange rates in the high-latitude E region ionosphere. *Journal of Geophysical Research: Space Physics*, *118*(11), 7369–7383. https://doi.org/10.1002/2013JA019195

Cai, L., Aikio, A. T., & Nygrén, T. (2014). Solar wind effect on Joule heating in the high-latitude ionosphere. *Journal of Geophysical Research: Space Physics*, *119*(12), 10440–10455. https://doi.org/10.1002/2014JA020269

Cheng, S., Yue, D., Yang, L., & Yue, X. (2017). Dependence of pedersen conductance in the E and F regions and their ratio on the solar and geomagnetic activities: Ionospheric conductance. *Space Weather-the International Journal of Research and Applications*, *15*(3), 484–494.

Davis, T. N., & Sugiura, M. (1966). Auroral electrojet activity index AE and its universal time variations. *Journal of Geophysical Research*, *71*(3), 785–801. https://doi.org/10.1029/JZ071i003p00785

Deng, Y., Fuller-Rowell, T. J., Ridley, A. J., Knipp, D., & Lopez, R. E. (2013). Theoretical study: Influence of different energy sources on the cusp neutral density enhancement. *Journal of Geophysical Research: Space Physics*, *118*(5), 2340–2349. https://doi.org/10.1002/jgra.50197

Deng, Y., Huang, Y., Lei, J., Ridley, A. J., Lopez, R., & Thayer, J. (2011). Energy input into the upper atmosphere associated with high-speed solar wind streams in 2005. *Journal of Geophysical Research*, *116*(A5). https://doi.org/10.1029/2010ja016201

Deng, Y., Maute, A., Richmond, A. D., & Roble, R. G. (2009). Impact of electric field variability on Joule heating and thermospheric temperature and density. *Geophysical Research Letters*, *36*(8), L08105. https://doi.org/10.1029/2008GL036916

Doornbos, E. (2012). *Thermospheric density and wind determination from satellite dynamics springer theses*. Springer-Verlag.

Emmert, J. T. (2015). Thermospheric mass density: A review. *Advances in Space Research*, *56*(5), 773–824. https://doi.org/10.1016/j.asr.2015.05.038

Fedrizzi, M., Fuller-Rowell, T. J., & Codrescu, M. V. (2012). Global Joule heating index derived from thermospheric density physics-based modeling and observations. *Space Weather*, *10*(3), S03001. https://doi.org/10.1029/2011SW000724

Fuller-Rowell, T. J., Codrescu, M. V., Moffett, R. J., & Quegan, S. (1994). Response of the thermosphere and ionosphere to geomagnetic storms. *Journal of Geophysical Research*, *99*(A3), 3893–3914. https://doi.org/10.1029/93JA02015

Fuller-Rowell, T. J., Codrescu, M. V., Roble, R. G., & Richmond, A. D. (2013). How does the thermosphere and ionosphere react to a geomagnetic storm? *Geophysical Monograph*, *98*, 203–225. https://doi.org/10.1029/GM098p0203

Gonzalez, W. D., Joselyn, J. A., Kamide, Y., Kroehl, H. W., Rostoker, G., Tsurutani, B. T., & Vasyliunas, V. M. (1994). What is a geomagnetic storm? *Journal of Geophysical Research*, *99*(A4), 5771–5792. https://doi.org/10.1029/93JA02867

Gonzalez, W. D., Tsurutani, B. T., & Gonzalez, A. L. C. D. (1999). Interplanetary origin of geomagnetic storms. *Space Science Reviews*, *88*(3–4), 529–562. https://doi.org/10.1023/a:1005160129098

Hardy, D. A., Gussenhoven, M. S., Raistrick, R., & Mcneil, W. J. (1987). Statistical and functional representations of the pattern of auroral energy flux and conductivity. *Journal of Geophysical Research*, *92*(A11), 12275–12294. https://doi.org/10.1029/ja092ia11p12275

Hedin, A. E. (1987). MSIS-86 thermospheric model. *Journal of Geophysical Research*, *92*(A5), 4649–4662. https://doi.org/10.1029/ja092ia05p04649

Hedin, A. E. (1991). Extension of the MSIS thermosphere model in the middle and lower atmosphere. *Journal of Geophysical Research*, *96*(A2), 1159–1172. https://doi.org/10.1029/90ja02125

Huang, Y., Richmond, A. D., Yue, D., & Roble, R. (2012). Height distribution of Joule heating and its influence on the thermosphere. *Journal of Geophysical Research*, *117*(A8), 8334. https://doi.org/10.1029/2012ja017885

Jacchia, L. G. (1971). New static models of the thermosphere and exosphere with empirical temperature profiles, Sao Special Report, *313*(20), 3138–3144.

Knipp, D., Kilcommons, L., Hairston, M., & Coley, W. R. (2021). Hemispheric asymmetries in Poynting flux derived from DMSP spacecraft. *Geophysical Research Letters*, *48*(17), e2021GL094781. https://doi.org/10.1029/2021GL094781

Knipp, D. J., Tobiska, W. K., & Emery, B. A. (2004). Direct and indirect thermospheric heating sources for solar cycles 21-23. *Solar Physics*, *224*(1), 495–505. https://doi.org/10.1007/s11207-005-6393-4

Krauss, S., Temmer, M., & Vennerstrom, S. (2018). Multiple satellite analysis of the earth's thermosphere and interplanetary magnetic field variations due to ICME/CIR events during 2003-2015. *Journal of Geophysical Research-Space Physics*, *123*(10), 8884–8894. https://doi.org/10.1029/2018ja025778

Kwak, Y.-S., Richmond, A. D., Deng, Y., Forbes, J. M., & Kim, K.-H. (2009). Dependence of the high-latitude thermospheric densities on the interplanetary magnetic field. *Journal of Geophysical Research*, *114*(A5), A05304. https://doi.org/10.1029/2008JA013882

Lei, J., Forbes, J. M., Liu, H.-L., Dou, X., Xue, X., Li, T., & Luan, X. (2011b). Latitudinal variations of middle thermosphere: Observations and modeling. *Journal of Geophysical Research*, *116*(A12), A12306. https://doi.org/10.1029/2011JA017067

Lei, J., Thayer, J. P., Forbes, J. M., Sutton, E. K., Nerem, R. S., Temmer, M., & Veronig, A. M. (2008). Global thermospheric density variations caused by high-speed solar wind streams during the declining phase of solar cycle 23. *Journal of Geophysical Research*, *113*(A11), A11303. https://doi.org/10.1029/2008JA013433

Lei, J., Thayer, J. P., Lu, G., Burns, A. G., Wang, W., Sutton, E. K., & Emery, B. A. (2011a). Rapid recovery of thermosphere density during the October 2003 geomagnetic storms. *Journal of Geophysical Research*, *116*(A3), A03306. https://doi.org/10.1029/2010JA016164

Liu, H., Lühr, H., Henize, V., & Köhler, W. (2005). Global distribution of the thermospheric total mass density derived from CHAMP. *Journal of Geophysical Research*, *110*(A4), A04301. https://doi.org/10.1029/2004JA010741

Lu, G., Richmond, A. D., Luhr, H., & Paxton, L. (2016). High-latitude energy input and its impact on the thermosphere. *Journal of Geophysical Research: Space Physics*, *121*(7), 7108–7124. https://doi.org/10.1002/2015JA022294

Lu, X., Liu, A. Z., Swenson, G. R., Li, T., Leblanc, T., & McDermid, I. S. (2009). Gravity wave propagation and dissipation from the stratosphere to the lower thermosphere. *Journal of Geophysical Research*, *114*(D11), D11101. https://doi.org/10.1029/2008JD010112

Lühr, H., Rother, M., Köhler, W., Ritter, P., & Grunwaldt, L. (2004). Thermospheric up-welling in the cusp region: Evidence from CHAMP observations. *Geophysical Research Letters*, *31*(6). https://doi.org/10.1029/2003gl019314

Ma, R., Xu, J., Wang, W., Lei, J., Liu, H.-L., Maute, A., & Hagan, M. E. (2010). Variations of the nighttime thermospheric mass density at low and middle latitudes. *Journal of Geophysical Research*, *115*(A12), A12301. https://doi.org/10.1029/2010JA015784

Maggiolo, R., Hamrin, M., De Keyser, J., Pitkänen, T., Cessateur, G., Gunell, H., & Maes, L. (2017). The delayed time response of geomagnetic activity to the solar wind. *Journal of Geophysical Research: Space Physics*, *122*(11), 11109–11127. https://doi.org/10.1002/2016JA023793

March, G., Doornbos, E., & Visser, P. (2018). High-fidelity geometry models for improving the consistency of CHAMP, GRACE, GOCE and Swarm thermospheric density data sets. *Advances in Space Research*, *63*(1), 213–238. https://doi.org/10.1016/j.asr.2018.07.009

March, G., van den IJssel, J., Siemes, C., Visser, P. N. A. M., Doornbos, E. N., & Pilinski, M. (2021). Gas-surface interactions modelling influence on satellite aerodynamics and thermosphere mass density. *Journal of Space Weather and Space Climate*, *11*, 54. https://doi.org/10.1051/swsc/2021035

March, G., Visser, T., Visser, P., & Doornbos, E. (2019). CHAMP and GOCE thermospheric wind characterization with improved gassurface interactions modelling. *Advances in Space Research*, *64*(6), 1225–1242. https://doi.org/10.1016/j.asr.2019.06.023

Miao, J., Liu, S., Zhitao, L. I., Huang, W., & Tang, G. (2012). Correlation of thermosphere density variation with different solar and geomagnetic indices. *Manned Spaceflight*, *18*(005), 24–30. https://doi.org/10.16329/j.cnki.zrht.2012.05.001

Moe, K., & Moe, M. M. (2005). Gas-surface interactions and satellite drag coefficients. *Planetary and Space Science*, *53*(8), 793–801. https://doi.org/10.1016/j.pss.2005.03.005

Oliveira, D. M., Zesta, E., Schuck, P. W., & Sutton, E. K. (2017). Thermosphere global time response to geomagnetic storms caused by coronal mass ejections. *Journal of Geophysical Research: Space Physics*, *122*(10), 10762–10782. https://doi.org/10.1002/2017JA024006

Palmroth, M., Grandin, M., Sarris, T., Doornbos, E., Tourgaidis, S., Aikio, A., et al. (2021). Lower-thermosphere–ionosphere (LTI) quantities: Current status of measuring techniques and models. *Annals of Geophysics*, *39*(1), 189–237. https://doi.org/10.5194/angeo-39-189-2021

Pardini, C., Moe, K., & Anselmo, L. (2012). Thermospheric density model biases at the 23rd sunspot maximum. *Planetary and Space Science*, *67*(1), 130–146. https://doi.org/10.1016/j.pss.2012.03.004

Picone, J. M., Hedin, A. E., Drob, D. P., & Aikin, A. C. (2002). NRL-MSISE-00 empirical model of the atmosphere: Statistical comparisons and scientific issues. *Journal of Geophysical Research*, *107*(A12), SIA-1–SIA15-16. https://doi.org/10.1029/2002ja009430

Redmon, R. J., Denig, W. F., Kilcommons, L. M., & Knipp, D. J. (2017). New DMSP database of precipitating auroral electrons and ions. *Journal of Geophysical Research: Space Physics*, *122*(8), 9056–9067. https://doi.org/10.1002/2016ja023339

Reigber, C., Lühr, H., & Schwintzer, P. (2002). CHAMP mission status. *Advances in Space Research*, *30*(2), 129–134. https://doi.org/10.1016/s0273-1177(02)00276-4

Rich, F. J., Gussenhoven, M. S., & Greenspan, M. E. (1987). Using simultaneous particle and field observations on a low altitude satellite to estimate joule heat energy flow into the high latitude ionosphere. *Annales Geophysicae*, *5*(6), 527–534.

Robinson, R., Vondrak, R., Miller, K., Dabbs, T., & Hardy, D. (1987). On calculating ionospheric conductances from the flux and energy of precipitating electrons. *Journal of Geophysical Research*, *92*(A3), 2565–2569. https://doi.org/10.1029/ja092ia03p02565

Rostoker, G., Akasofu, S.-I., Foster, J., Greenwald, R., Kamide, Y., Kawasaki, K., et al. (1980). Magnetospheric substorms—definition and signatures. *Journal of Geophysical Research*, *85*(A4), 1663–1668. https://doi.org/10.1029/JA085iA04p01663

Ruan, H., Lei, J., Dou, X., Liu, S., & Aa, E. (2018). An exospheric temperature model based on CHAMP observations and TIEGCM simulations. *Space Weather*, *16*(2), 147–156. https://doi.org/10.1002/2017SW001759

Srivastava, N., & Venkatakrishnan, P. (2004). Solar and interplanetary sources of major geomagnetic storms during 1996-2002. *Journal of Geophysical Research*, *109*(A10), A10103. https://doi.org/10.1029/2003ja010175

Storz, M. F., Bowman, B. R., Branson, M. J. I., Casali, S. J., & Tobiska, W. K. (2005). High accuracy satellite drag model (HASDM). *Advances in Space Research*, *36*(12), 2497–2505. https://doi.org/10.1016/j.asr.2004.02.020

Sugiura, M. (1964). *In annals of the international geophysical year* (Vol. 35, pp. 7–45). Oxford: Pergamon Press.*Hourly values of equatorial Dst for IGY*.

Sutton, E. K., Cable, S. B., Lin, C. S., Qian, L., & Weimer, D. R. (2012). Thermospheric basis functions for improved dynamic calibration of semi-empirical models. *Space Weather-the International Journal of Research & Applications*, *10*(10). https://doi.org/10.1029/2012sw000827

Sutton, E. K., Forbes, J. M., & Knipp, D. J. (2009). Rapid response of the thermosphere to variations in Joule heating. *Journal of Geophysical Research*, *114*(A4), A04319. https://doi.org/10.1029/2008JA013667

Tapley, B. D., Bettadpur, S., Watkins, M., & Reigber, C. (2004). The gravity recovery and climate experiment: Mission overview and early results. *Geophysical Research Letters*, *31*(9). https://doi.org/10.1029/2004gl019920

Thayer, J. P., Vickrey, J. F., Heelis, R. A., & Gary, J. B. (1995). Interpretation and modeling of the high-latitude electromagneticenergy flux. *Journal of Geophysical Research*, *100*(October), 19715–19728. https://doi.org/10.1029/95ja01159

Vallado, D. A., & Finkleman, D. (2014). A critical assessment of satellite drag and atmospheric density modeling. *Acta Astronautica*, *95*, 141–165. https://doi.org/10.1016/j.actaastro.2013.10.005

Van den IJssel, J., Doornbos, E., Iorfida, E., March, G., & Montenbruck, O. (2020). Thermosphere densities derived from Swarm GPS observations. *Advances in Space Research*, *65*(7), 1758–1771. https://doi.org/10.1016/j.asr.2020.01.004

Wang, X., Miao, J., Aa, E., Ren, T., Wang, Y., Liu, J., & Liu, S. (2020b). Statistical analysis of Joule heating and thermosphere response during geomagnetic storms of different magnitudes. *Journal of Geophysical Research: Space Physics*, *125*(8), e2020JA027966. https://doi.org/10.1029/2020JA027966

Wang, X., Miao, J., Liu, S. Q., & Ren, T. L. (2020a). Characteristics analysis of thermospheric density response during the different intensity of geomagnetic storms. *Chinese Journal of Space Science*, *40*(1), 28–41.

Wang, X., Miao, J., Xian, L., Aa, E., Wang, Y., Liu, J., & Liu, S. (2021). Latitudinal impacts of joule heating on the high-latitude thermospheric density enhancement during geomagnetic storms. *Journal of Geophysical Research: Space Physics*, *126*(7). https://doi.org/10.1029/2020ja028747

Weimer, D. R. (2001). An improved model of ionospheric electric potentials including substorm perturbations and application to the Geospace Environment Modeling November 24, 1996, event. *Journal of Geophysical Research*, *106*(A1), 407–416. https://doi.org/10.1029/2000ja000604

Weimer, D. R. (2005). Improved ionospheric electrodynamic models and application to calculating joule heating rates. *Journal of Geophysical Research*, *110*(A5), A05306. https://doi.org/10.1029/2004ja010884

Weng, L., Lei, J., Sutton, E., Dou, X., & Fang, H. (2017). An exospheric temperature model from CHAMP thermospheric density. *Space Weather*, *15*(2), 343–351. https://doi.org/10.1002/2016SW001577

Wilson, G. R., Weimer, D. R., Wise, J. O., & Marcos, F. A. (2006). Response of the thermosphere to Joule heating and particle precipitation. *Journal of Geophysical Research*, *111*(A10), A10314. https://doi.org/10.1029/2005ja011274

Wu, H., Lu, X., Lu, G., Chu, X., Wang, W., Yu, Z., et al. (2020). Importance of regional-scale auroral precipitation and electrical field variability to the storm-time thermospheric temperature enhancement and inversion layer (TTEIL) in the Antarctic E region. *Journal of Geophysical Research: Space Physics*, *125*(9), e2020JA028224. https://doi.org/10.1029/2020JA028224

Xu, J., Wang, W., Lei, J., Sutton, E. K., & Chen, G. (2011). The effect of periodic variations of thermospheric density on CHAMP and GRACE orbits. *Journal of Geophysical Research*, *116*(A2), A02315. https://doi.org/10.1029/2010JA015995

Xu, J., Wang, W., Zhang, S., Liu, X., & Yuan, W. (2015). Multiday thermospheric density oscillations associated with variations in solar radiation and geomagnetic activity. *Journal of Geophysical Research: Space Physics*, *120*(5), 3829–3846. https://doi.org/10.1002/2014JA020830

Zesta, E., & Huang, C. Y. (2016). Satellite orbital drag. In G. V. Khazanov (Ed.), *Space weather fundamentals* (pp. 329–351). CRC Press.

Zesta, E., & Oliveira, D. M. (2019). Thermospheric heating and cooling times during geomagnetic storms, including extreme events. *Geophysical Research Letters*, *46*(22), 12739–12746. https://doi.org/10.1029/2019GL085120

Zhang, B. C., Kamide, Y., Liu, R. Y., Shinagawa, H., & Iwamasa, K. (2004). A modeling study of ionospheric conductivities in the high latitude electrojet regions. *Journal of Geophysical Research*, *109*(A4), A04310. https://doi.org/10.1029/2003JA010181

Zhang, S.-R., Erickson, P. J., Coster, A. J., Rideout, W., Vierinen, J., Jonah, O. F., & Goncharenko, L. P. (2019). Subauroral and polar traveling ionospheric disturbances during the 7–9 September 2017 storms. *Space Weather*, *17*(12), 1748–1764. https://doi.org/10.1029/2019SW002325

Zhou, Y. L., Ma, S. Y., Lühr, H., Xiong, C., & Reigber, C. (2009). An empirical relation to correct storm-time thermospheric mass density modeled by NRLMSISE-00 with CHAMP satellite air drag data. *Advances in Space Research*, *43*(5), 819–828. https://doi.org/10.1016/j.asr.2008.06.016